Bulletin of the Seismological Society of America, Vol. 84, No. 6, pp. 1786–1800, December 1994

Ground-Motion Amplitude Across Ridges

by H. Pedersen, B. Le Brun, D. Hatzfeld, M. Campillo, and P.-Y. Bard

Abstract Local amplification and wave diffraction on an elongated ridge near Sourpi in central Greece were studied by the analysis of seismic records of local and regional earthquakes. Data were obtained during field work especially designed for this purpose. These data were analyzed in the frequency and time domains. In the frequency domain, spectral ratios show amplifications of 1.5 to 3 at the ridge top relative to the base of the ridge. The horizontal components of motion are more amplified than the vertical component and the observed spectral ratios seem stable for different earthquake locations. Theoretical spectral ratios, calculated by the indirect boundary element method, are dependent on earthquake location but are in general agreement with the observed spectral ratios. Another dataset, from Mont St. Eynard in the French Alps, showed similar characteristics with spectral amplitudes on the top of the ridge up to four times those on the flank. These relative amplifications are within the range predicted by numerical simulations. The numerical simulations also show that the topographic effect involves the emission of diffracted waves propagating from the top toward the base of the ridge. The use of a seven-station array on the ridge at Sourpi made it possible to identify such waves. The analysis was performed with wave separation methods using singular value decomposition and spectral matrix filtering. Our results show agreement between experimental data and theoretical results supporting the use of numerical simulations for estimation of purely topography-induced amplification on ridge tops. Our results also show that such amplification is moderate for the ridges under study.

Introduction

Over the last 2 decades, topographic effects on seismic waves have received increasing interest as a result of some observations of large amplification on mountain tops, combined with the importance of some of the structures typically built on elevated topographies (e.g., communication and power supply pylons).

Very high accelerations recorded at Pacoima Dam during the San Fernando earthquake of 1971 (Trifunac and Hudson, 1971; Boore, 1973) and the damage pattern during the 1987 Whittier Narrows earthquake (Kawase and Aki, 1990) have been at least partly attributed to site effects. Observations of amplification on top of mountains have been reported by several authors (e.g., Davis and West, 1973; Griffiths and Bollinger, 1979; Bard and Tucker, 1985; Çelebi, 1987; Umeda *et al.*, 1987). Common to most of these studies is the fact that the observations have not been explained by numerical simulations. The simulations and the observations are in qualitative agreement on an amplification of seismic waves on the top of the topography for wavelengths comparable to mountain width. The disagreement between observations and simulations concerns primarily the level of amplification of ground motion. Simulations predict displacements of up to twice the displacements of the free field, i.e., the displacement in absence of the topography. Observations show that the level of amplification can be significantly higher (exceeding a factor of 10). At the slopes and base of the mountain, numerical simulations predict that amplification and deamplification alternate as a function of frequency. This means in practice that amplification on mountain tops estimated by comparison with a reference station at the base can be severely biased.

Most simulations of topographic effects are performed for isolated ridges or canyons over a homogeneous half-space (e.g., Bouchon, 1973; Wong and Jennings, 1975; Bard, 1982; Sánchez-Sesma *et al.*, 1982; Wong, 1982; Bouchon, 1985; Sánchez-Sesma *et al.*, 1985; Kawase, 1988; Luco *et al.*, 1990; Sánchez-Sesma and Campillo, 1991, 1993). The discrepancy between observations and numerical simulations may be due to a complex geology beneath the mountain, a complicated incident wave field, or a more complex topography than the ones introduced in the models; e.g., subsurface lay-

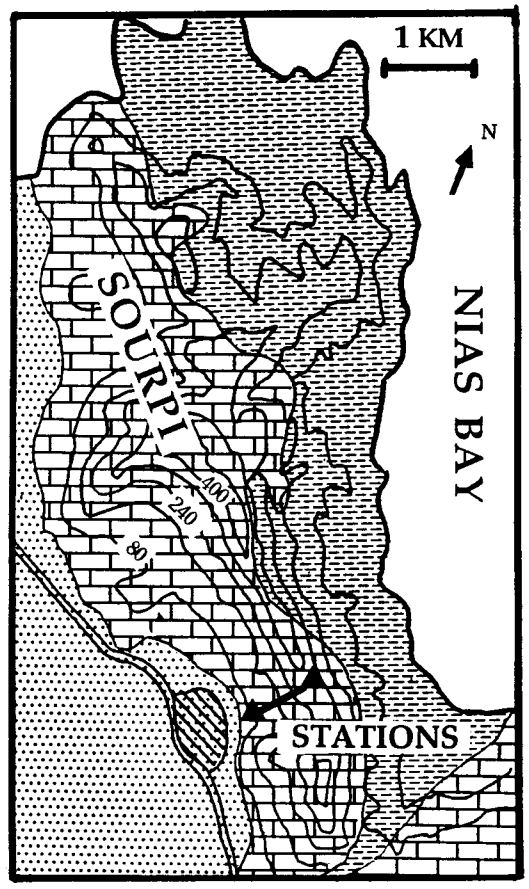

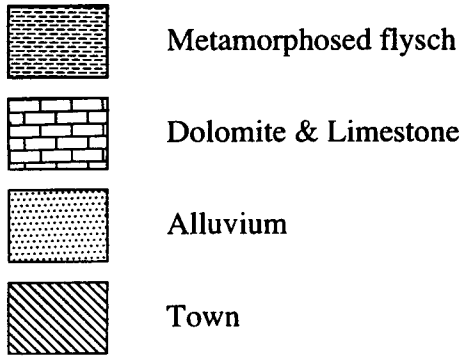

(a)

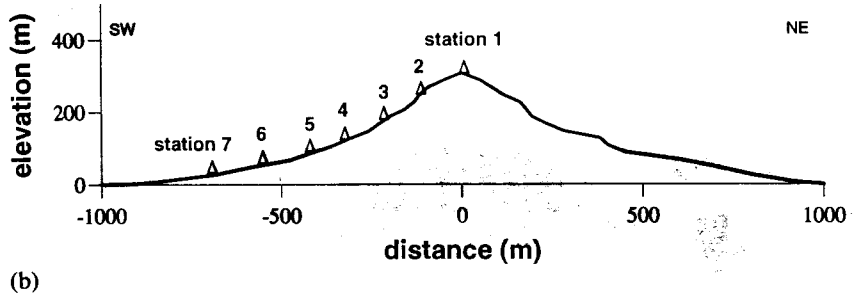

(b)

Figure 1. Geometry of Sourpi and seismological stations (triangles). (a) Geological and contour map (altitude in meters). (b) Topographic cross section and seismic stations.

ering (Bard and Tucker, 1985; Geli *et al.*, 1988), neighboring topography (Geli *et al.*, 1988), or three-dimensional (3D) effects (Sánchez-Sesma, 1983; Pedersen *et al.*, 1994). This explanation is supported by the fact that for model studies (Rogers *et al.*, 1974; Anooshepoor and Brune, 1989), theoretical predictions and observations seem to be in good agreement.

This study is an attempt to model observed site effects across ridges. Our intention is to show that there indeed exist cases with quantitative agreement between observations and theoretical predictions and that amplification at a mountain top is not systematically high.

Data were obtained during field work especially designed to study site effects due to topographies. The main ridge under study was chosen because the medium below is rather homogeneous, with hardly any overburden, so data can be compared with numerical simulations for simple, two-dimensional models.

Results from this field work will be presented, as well as comparisons with numerical simulations. The use of a seven-station array made it possible to analyze the signals thoroughly in both the frequency and the time domain. In the time domain, data were analyzed particularly to identify the diffracted waves in the seismic records. Selected results are also presented for a dataset from an extremely steep ridge to investigate whether an extreme topography may induce very large amplifications.

Field Work and Data Selection

The main ridge of this study is located near Sourpi, about 30 km south of Volos in central Greece. This region has experienced complex tectonic deformation since the Miocene time (Mercier *et al.*, 1976). The ridge (subsequently referred to as "Sourpi") is a fold of 400-m-thick Middle Triassic-Jurassic limestone with a homogeneous surface geology, according to geological maps of the area, and confirmed by surface observations made during the field work. The limestone is underlain by metamorphosed Permian graywackes and shales, and it is overlain by a thin layer of metamorphosed Upper Cretaceous flysch at the northeastern side of the ridge. The soil cover is very thin (0 to 20 cm) with limestone outcrops at the surface. Sourpi is oriented NW–SE, and is about 5-km long, 2.5-km wide, and 300-m high. Figure 1a shows the geological units of the area, and a cross

section perpendicular to the ridge is shown in Figure 1b. Because the ridge is significantly longer than it is wide, we will assume that it is two dimensional in the numerical simulations.

Seven seismological stations were installed along a profile perpendicular to the topography (see Fig. 1). They were buried in holes down to hard rock to avoid site effects from surface soil and reduce noise due to the wind. The distance between stations was estimated and the altitude was measured with an altimeter so the station locations could be plotted on a detailed topographic map. The seismometers were 3D Mark Product L4C with a natural frequency of 2 Hz, and they were connected to a digital data logger HADES-TITAN with a sampling rate of 100 samples/sec. The dynamic range was 16 bits and the effective dynamic range of the signal was 10 bits. The internal clock was synchronized by an external radio (DCF) time signal and the time was measured with an uncertainty of less than 0.01 sec.

Fourteen local and regional shallow earthquakes recorded with a signal to noise ratio over five for the *S* waves and their coda (typically between ten and 100 for frequencies between 1 and 10 Hz) were selected for analysis. Only three of these 14 events were recorded on all stations. Figure 2 shows a map of the earthquake epicenters. With one exception, no earthquakes occurred to the south or the southwest. Otherwise, the epicenters are distributed quite evenly around the ridge.

Observed Spectral Ratios

For the analysis in the frequency domain, the station located at the base of the ridge (station 7) was selected as a reference station. For the three components of motion, spectral ratios were calculated between stations 1 through 6 and station 7 for the 14 events. The time window (of 8- to 20-sec length, depending on the signal to noise ratio) used for the calculations comprised the *S* arrival and coda *S*. Tests showed that the spectral ratios were almost independent of the time window applied within the *S* wave train. The spectral amplitude ratio was calculated between the spectra smoothed with a 2-Hz-wide running window.

Figure 3 shows all spectral ratios calculated between station 1 and 7 as well as the smoothed average for each component. There is considerable scatter between curves

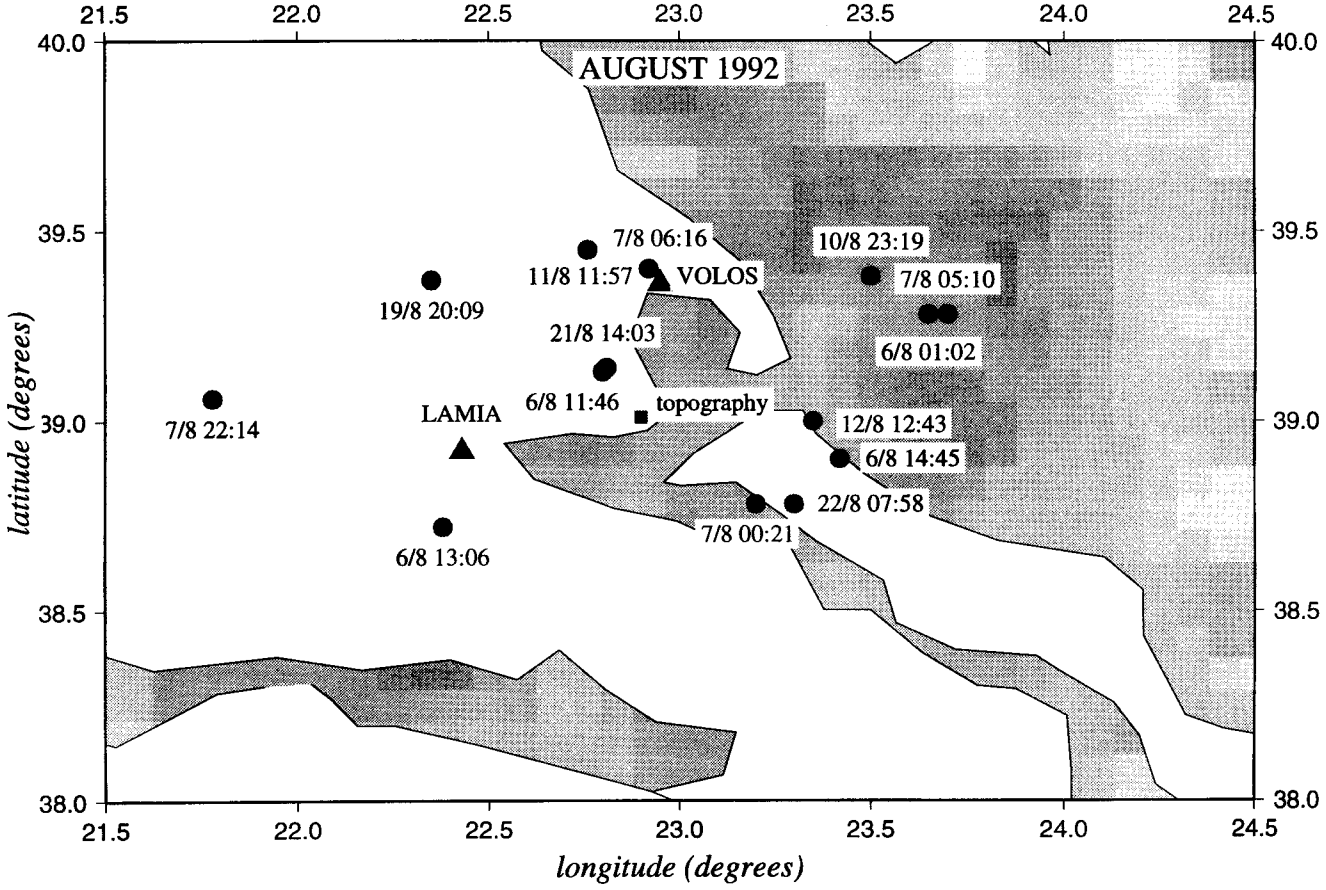

Figure 2. Location map of seismic events (solid circles) recorded at Sourpi. The Sourpi area is indicated by a square in the center of the map. Towns are shown by triangles.

for different events but this scatter cannot be directly related to the locations of seismic events. The average spectral ratios are maximum 2.5 for the N–S component, 2 for the E–W component, and 1.5 for the *Z* component, and peaks significantly exceeding the average values were due to low spectral amplitudes at the reference station. Figure 4 shows the average spectral ratios with their standard deviations for stations 1, 3, and 6. For the horizontal components, the observed amplifications relative to station 7 increase with altitude, while there is no clear altitude effect on the *Z* component.

Theoretical Spectral Ratios

Simulations were performed to assess how the topography influences the seismic wave field in the frequency and the time domain. The method used for the simulations was the indirect boundary element method (IBEM), extended to the case of 3D scattering by two-dimensional (2D) topographies (Pedersen *et al.*, 1994). It has the advantage of simulating the total wave field without any inherent assumptions and can in principle be applied at all frequencies. The simulation is carried out in the frequency domain. Time domain solutions are obtained by multiplication with a source function followed by a Fourier transform.

The incident wave field can be plane *P*, *SH*, *SV*, or Rayleigh waves. It can have an arbitrary azimuth ϕ and a vertical incidence θ to the structure. The azimuth is defined as the angle between the incoming wave and the x axis (see Fig. 5a), and the vertical incidence as the angle between the incoming wave and the z axis (see Fig. 5b). Azimuths of 0° and 180° correspond to incoming waves in the 2D plane from the southeast and northwest.

The model used in the simulations is that of an infinitely long topography with a cross-sectional shape that corresponds to that of Sourpi at the profile through the seismic stations (see Fig. 1). The Earth displacement is simulated at 101 points across the topography. All

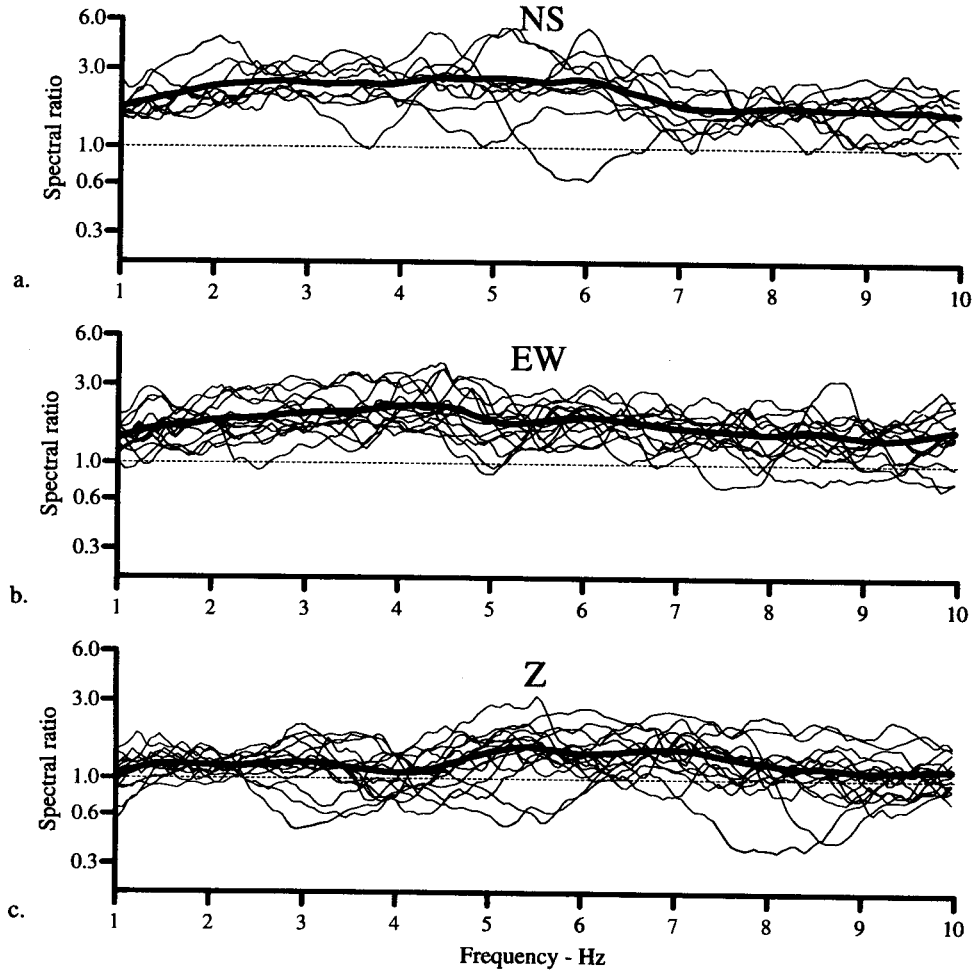

Figure 3. Spectral ratios station 1/station 7 at Sourpi. (a) N–S component (nine measurements). (b) E–W component (14 measurements). (c) Z component (14 measurements).

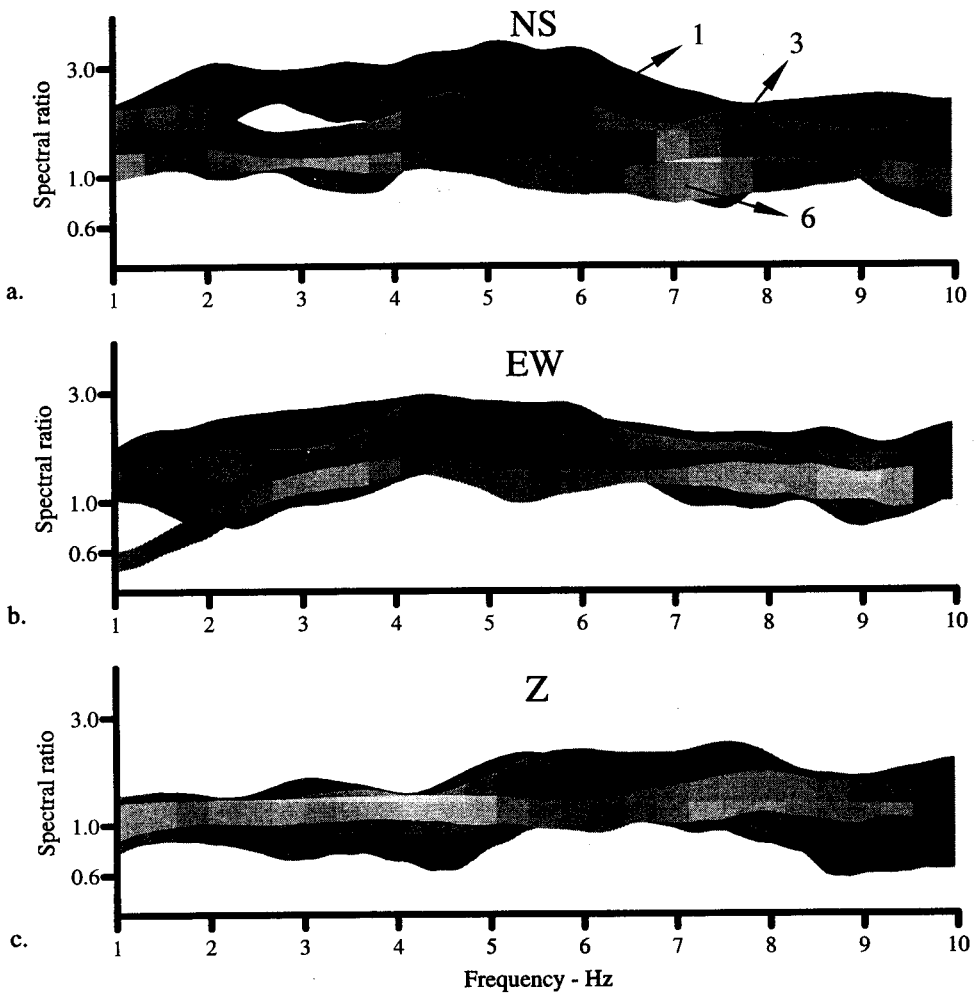

Figure 4. Dependence of altitude on spectral amplitudes. The shaded areas represent the average spectral ratios relative to station 7 and their standard deviations. Black: station 1. Dark grey: station 3. Light grey: station 6. (a) N–S component. (b) E–W component. (c) *Z* component.

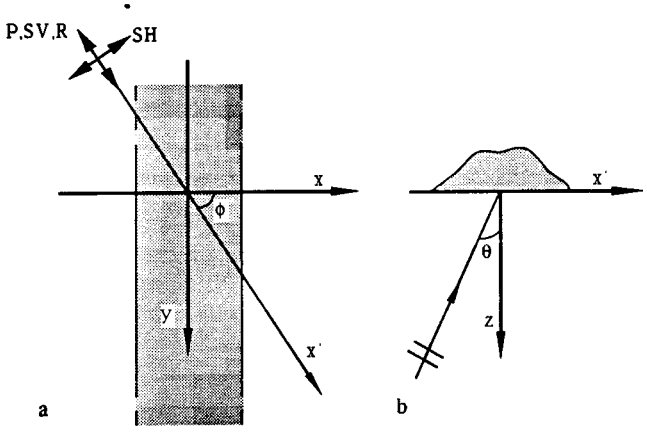

Figure 5. Definition of azimuth and incidence. (a) Definition of azimuth ϕ, horizontal plane. (b) Definition of incidence θ, vertical plane.

neighboring topographies are ignored. The medium below the topography is assumed to be homogeneous with a compressional wave velocity of 4.8 km/sec and a shear-wave velocity of 2.8 km/sec. These wave velocities were estimated based on values for limestone in the area. In the numerical simulations, changes in wave velocities used in the models only cause simple shifts in the frequency of the amplification. For example, a reduction of 10% in the wave velocities implies that an amplification previously at 10 Hz would be shifted to 9 Hz.

An example of a theoretically calculated spectral ratio between station 1 and 7 for the N–S component is shown in Figure 6. The example is that of an incoming *SV* wave with azimuth 60° and incidence 30°, for which the amplitude of N–S motion would be 0.63 in absence of the topography. Amplitudes at station 1 and 7 are shown

by the dotted and dashed lines and the spectral ratio between the two is the solid line. Ground motion is amplified moderately (1.5 to 2-fold) at station 1 and is amplified or deamplified at station 7. The spectral ratio can be up to ten at frequencies where there is deamplification at station 7, and the ratio is at most frequencies significantly higher than absolute amplification. The influence of deamplification on the spectral ratios at the reference station seemed to be common for all the simulations. The amplifications and deamplifications across the ridge are highly azimuth dependent (e.g., Pedersen *et al.*, 1994), showing that spectral ratios are very sensitive to changes in azimuth.

Figure 7 is a comparison of theoretical spectral ratios (lines) and observed spectral ratios plus or minus one standard deviation (shaded areas) between station 1 and 7 for the N–S, E–W, and Z component. The lines correspond to different azimuths (ϕ = 0°, 30°, 60°, ..., 180°) used in the simulations and the incident waves are of type *SV*. High spectral ratios due to deamplifications made it difficult to directly compare theoretical spectral ratios with observed ones, so the theoretical spectral ratios were stabilized by adding the energy for two incidence angles (45° and 60°). The spectral ratio was found as the square root of the ratio top/base of added energies.

The observed level of relative amplification is within the range predicted by theory. Large angles of incidence are expected because the earthquakes are shallow (0 to 10 km), but the incident wave field is also expected to be very complex in the time window (*S* waves and coda *S*) for which the spectral ratios were calculated. One possibility to take this into account in the theoretical spectral ratios is to integrate results for different incidence angles, wave types, and azimuths, but we do not have sufficient knowledge about the incident waves for the application of such an integration. The stabilizing effect of adding energy for different incidence angles nevertheless confirms that observed spectral ratios may be an "averaged" measure of the response of the topography.

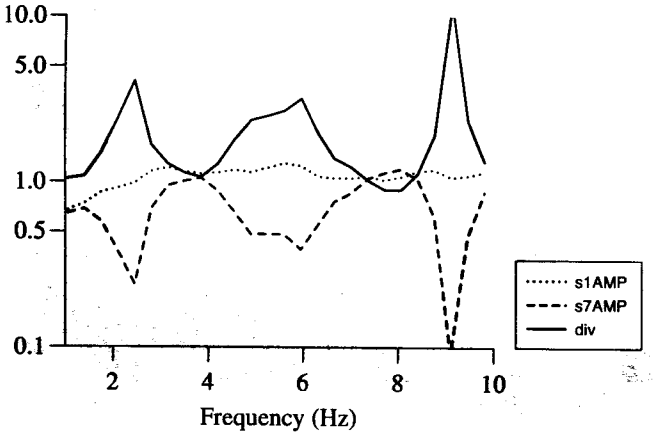

Figure 6. Example of spectral amplitudes and spectral ratio of the N–S component calculated from numerical simulations. The incoming waves are of type *SV* with an azimuth of 60° and incidence of 30°. Dotted line: amplitude at station 1. Dashed line: amplitude at station 7. Continuous line: spectral ratios station 1/station 7.

Identification of Diffracted Waves

Figure 8 shows an example of simulation where the incident waves are of type *SV*, have an azimuth of 200°, and an incidence angle of 30°. The source function is a Ricker wavelet of 4.2-Hz central frequency. The example was chosen to illustrate a general feature of the simulations: the emission of a diffracted wave from the top of the ridge. The actual focusing of energy may not necessarily take place at the surface, but can possibly take place at some depth beneath the top of the ridge and it can be shifted horizontally depending on the frequency, azimuth, and incidence angle of the incident waves. The propagation time of the diffracted wave between the top and the base is typically around 0.4 sec, which corresponds to an apparent velocity perpendicular to the ridge of 2.5 km/sec. In most of the simulations, amplification exists near the top of the ridge or on the uppermost part of the flank, possibly due to focusing of energy and constructive interference between the incident and the diffracted waves.

Figure 9 shows an example of a similar amplification in data. It shows the seismograms of the horizontal component orthogonal to the ridge, i.e., after rotation of the horizontal components N–S and E–W by 45°. There is clearly a relative amplification of the seismic signal at the top of the ridge compared to other positions. This result is a time domain equivalent of the spectral amplifications shown in Figure 4. In all cases, the amplification was modest, typically approximately 1.5 to 2.

According to these numerical simulations, the fact that records from the stations in the array are not identical (except for time shifts) can be grossly explained by the focusing of energy near the top of the ridge and superposition of the incident wave field with diffracted waves that are continuously emitted with an amplitude proportional to the amplitude of the incident waves. The two phases propagate with different apparent velocities across the array. Identification of the diffracted waves is nevertheless difficult, as the diffracted waves have a small amplitude. They will, therefore, be hidden by the incident waves that have a higher amplitude and a long time duration. Methods that are particularly adapted to wave separation are therefore necessary for the identification of diffracted waves.

The following analysis consists of an extraction of the incident waves from the records by use of a singular value decomposition (SVD) of the data followed by an

extraction of the strongest-amplitude propagating wave present in the residual by spectral matrix filtering (SMF). In the following, SVD and SMF are briefly presented.

SVD (e.g., Lines and Treitel, 1984; Freire *et al.*, 1988; Glangeaud and Mari, 1993, 1994) is a singular value decomposition of the data. It operates in the time domain and is a very efficient method for extraction of seismic waves that arrive simultaneously on all records (Glangeaud and Mari, 1993, 1994). The data matrix **R** (of dimension $nr \times nt$, where nr is the number of records and nt the number of samples) can be decomposed by

$$\mathbf{R} = \mathbf{V}\Lambda\mathbf{U}^{+} = \sum_{j=1}^{ns} \sqrt{\lambda_j}\vec{v}_j\vec{u}_j^{+},$$

where **V** is the matrix of eigenvectors of $\mathbf{RR}^{+}$, **U** the nr left columns of the matrix of eigenvectors of $\mathbf{R}^{+}\mathbf{R}$, Λ is the matrix of eigenvalues, and $^{+}$ denotes complex transpose. The first eigensection of SVD corresponds to $j = 1$, when the eigenvalues are sorted in decreasing order. The optimal way to use SVD (Glangeaud and Mari, 1993, 1994) is to perfectly align the waves to be extracted, apply SVD, and extract the waves as the first eigensection. This procedure can be repeated on the residual (data − first eigensection).

SMF (Mermoz, 1976; Glangeaud and Latombe, 1983) operates in the frequency domain, where records are projected on the eigenvectors of the spectral matrix. It is more efficient than SVD when the waves do not arrive simultaneously on all records. It is nevertheless preferable not to have too significant shifts of the signals because they influence the calculation of the spectral matrix, which is found as an average of cross spectra in the frequency domain. SMF has been used for analysis of seismic signals by, e.g., Glangeaud and Lacoume (1985), Mars *et al.* (1987), Nicollin *et al.* (1988), and Campillo *et al.* (1988).

Prior to analysis by SVD and SMF, the records were whitened (i.e., their spectra flattened and normalized) to

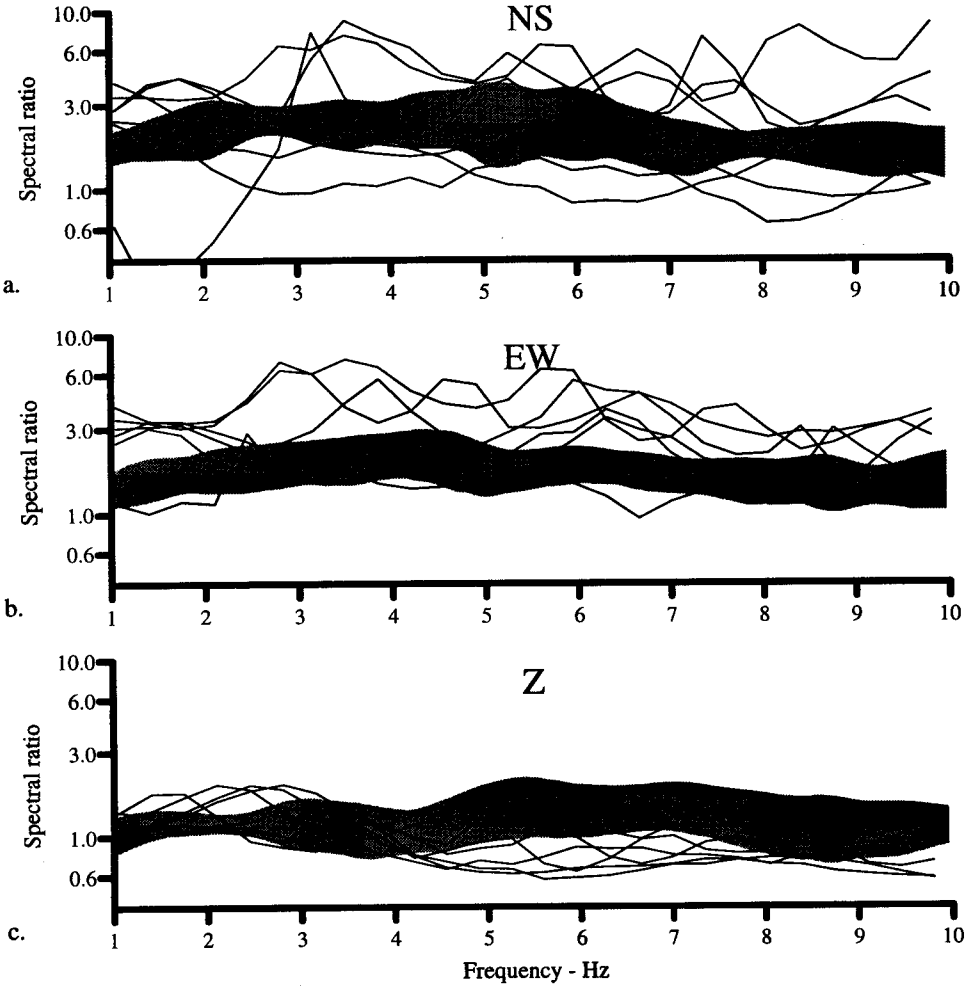

Figure 7. Comparison of theoretical spectral ratios (solid lines) and observed spectral ratios plus or minus one standard deviation (shaded area).

give equal weight to each record and bandpassed 2 to 6 Hz to avoid high-frequency noise. The normalization of the records is essential to the analysis and both whitening and normalization by peak spectral amplitude give good results. The rest of the analysis consisted of the following steps.

1. Shifting the traces so major peaks are aligned.
2. Extracting the incident waves as the first eigensection of SVD.
3. Aligning approximately the peaks in the residual signal of SVD (data − first eigensection).
4. Applying SMF and extracting the first eigensection.

Only three events were recorded on all stations. Parts of these records were analyzed by the method presented above. For each event, the vertical and the horizontal component perpendicular to the topography were analyzed. One or two stations were excluded from analysis due to problems with the time synchronization. Short time windows were applied to select the *P* arrival and the *S* arrival because they potentially have clear peaks for the alignment prior to SVD. Seven out of the 12 datasets were rejected because of low amplitudes or because of low coherency between signals that would make it difficult to extract the incident wave field. For one event (22/8 at 07:58) the *P*-wave window was analyzed on the N–S component because the perpendicular component to the topography coincided with the transverse component relative to the path between the source and receiver.

After analysis, diffracted waves were easily identified on four out of the five datasets. *S* and *P* waves seemed to be equally well adapted for the analysis with two successful identifications in the *S*-wave window and two in

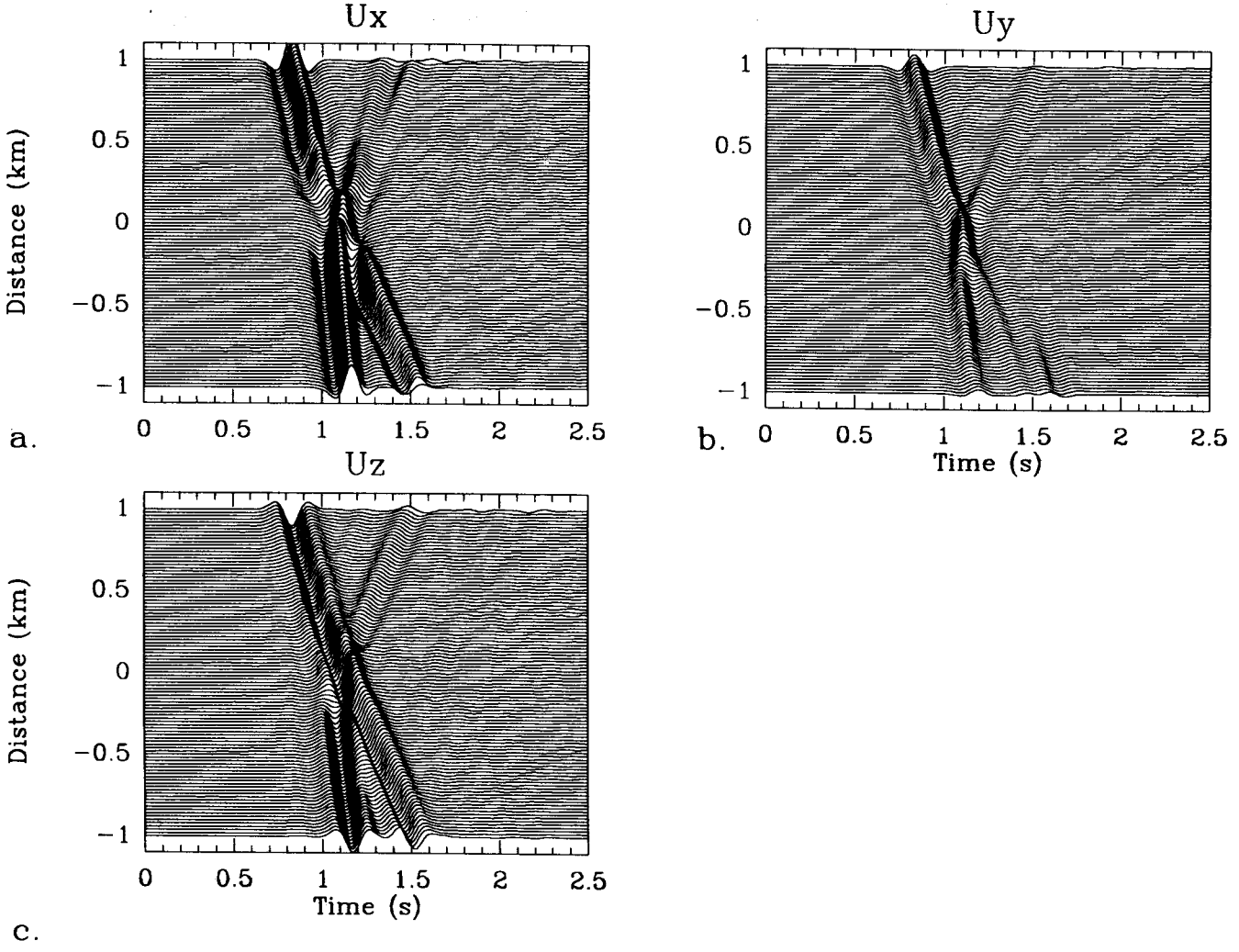

Figure 8. Example of synthetic seismograms across Sourpi for incident *SV* waves with azimuth 200° and incidence 30°. (a) Horizontal component perpendicular to topography. (b) Horizontal component parallel to topography. (c) Vertical component.

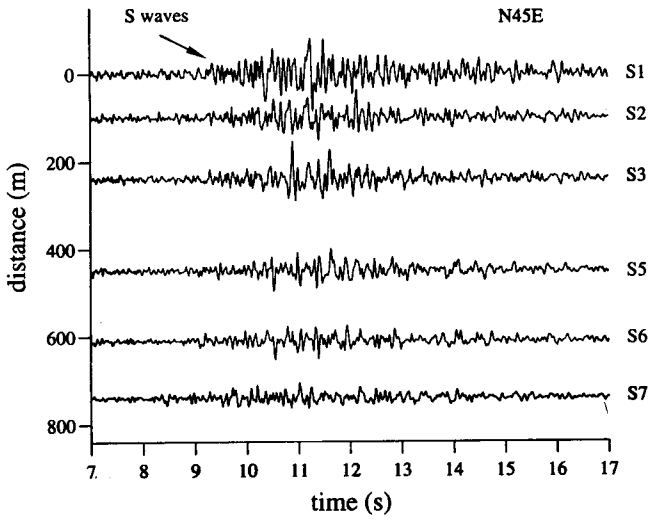

Figure 9. Example of amplification at Sourpi ridge-top: perpendicular component (N45°E) of event 920806 at 13:06.

the *P*-wave window. Two of the identifications were made on the orthogonal component, one on the N–S component, and one on the vertical component. Figures 10 and 11 show two examples of analysis. The figures present the bandpass-filtered (2 to 6 Hz) records used in the analysis (Figs. 10a and 11a) as well as the extracted incident waves (Figs. 10b and 11b), the first eigensection of SMF (Figs. 10c and 11c), and the residual signal after application of SMF (Figs. 10d and 11d). In the figures, the results are corrected for whitening and alignment of the signals used during the analysis so the processed signals (Figs. 10b through 10d, 11b through 11d) can be directly compared to the input signals (Figs. 10a and 11a). The maximum amplitude of the first trace compared to that of the first trace in data is given in each seismic section for comparison.

The extracted incident waves account as expected for a major part of the records (Figs. 10b and 11b) while the maximum amplitude in the first eigensection of SMF (Figs. 10c and 11c) is only 20% and 16% of that of the

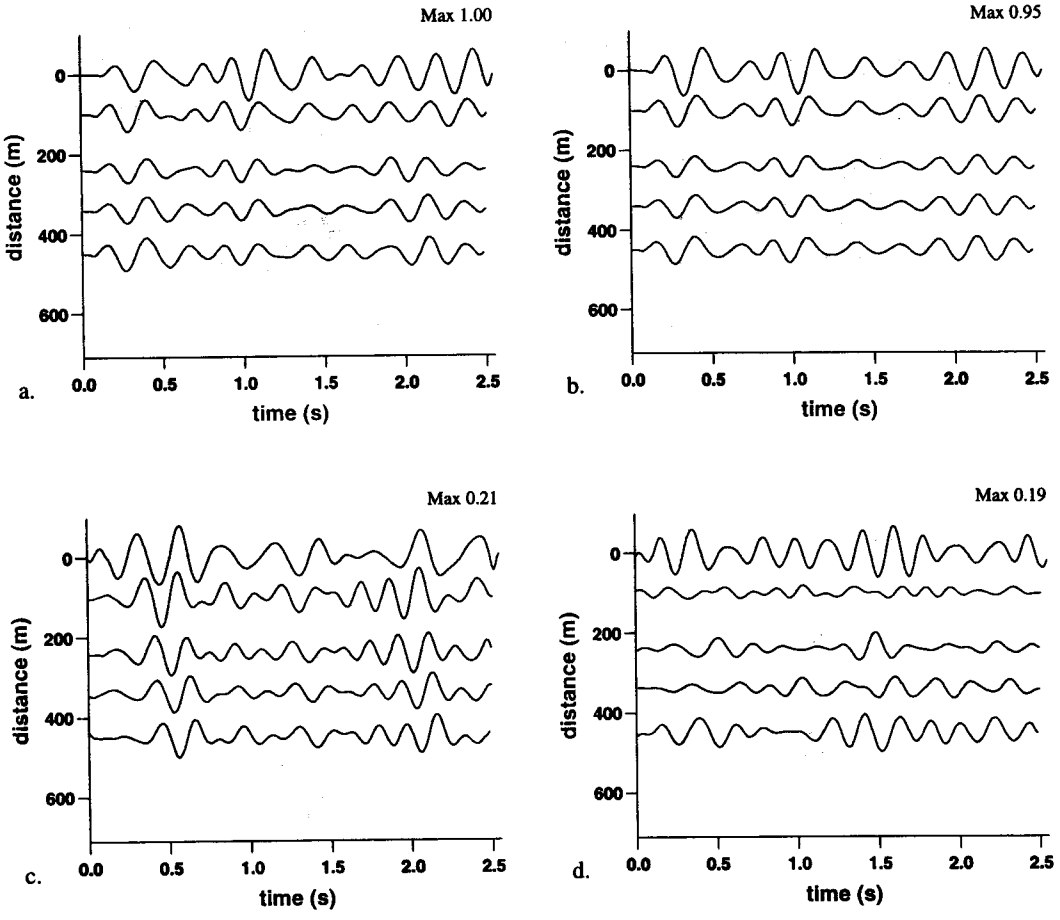

Figure 10. Example of identification of diffracted waves by SVD-SMF analysis: N–S component, window on *P* arrival, event 920821 at 07:58 (a) Data used in the analysis. (b) first eigensection of SVD. (c) first eigensection of SMF. (d) Residual after SMF.

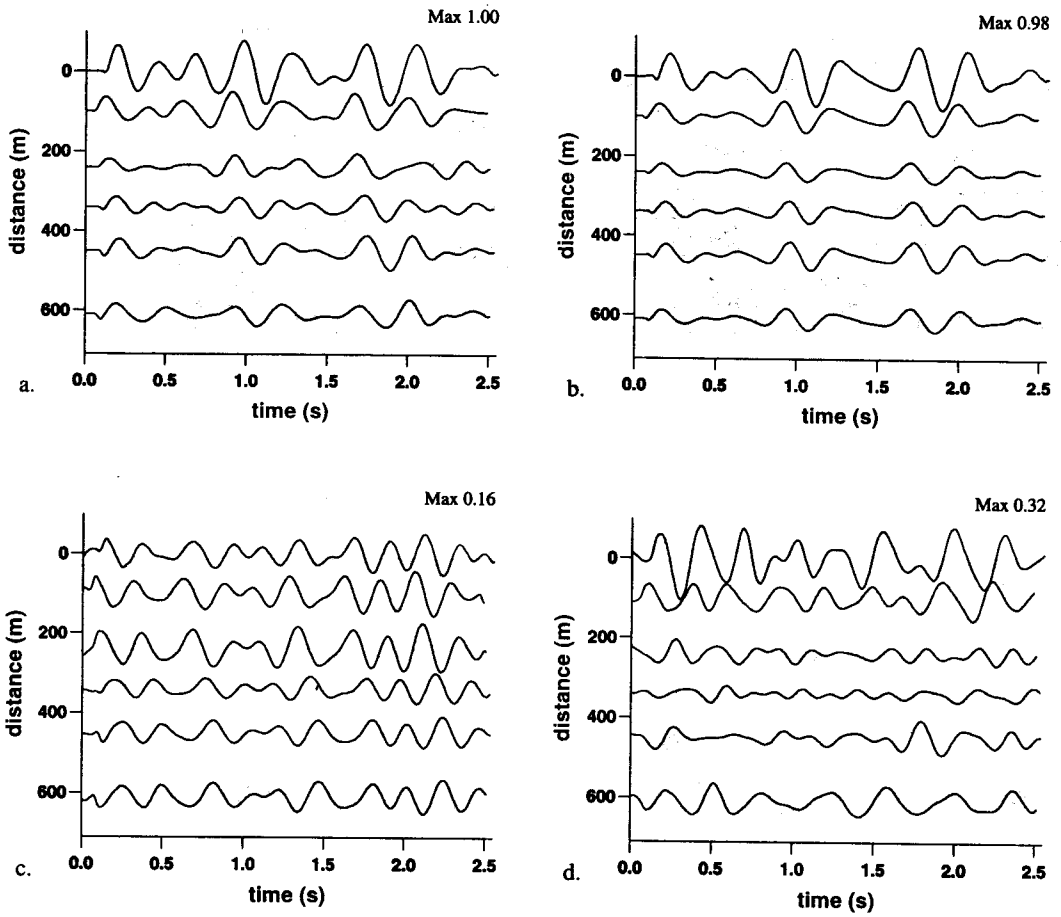

Figure 11. Same as Figure 9, for a perpendicular component for a window on *S* arrival, event 920811 at 11:57.

data. This is the same order of magnitude as the amplitudes of diffracted waves in the simulations, where the amplitudes depend on the incident waves (type, azimuth, incidence). The first eigenvalue of SMF is in both cases approximately 2.5 times bigger than the second eigenvalue for all frequencies between 2 and 6 Hz. The SMF first eigensections show the characteristics that one would expect if they consisted of diffracted waves: the waves propagate across the array with an apparent velocity of approximately 3 km/sec and have a small but significant amplitude compared to the incident waves. The seismic sections that correspond to the residual signal of SMF (i.e., data − first eigensection of SVD − first eigensection of SMF) (Figs. 8d and 9d) consist of signals that seem incoherent across the seismic section. Further extraction of waves would not be reliable as the second eigenvalue of SMF is small.

The propagation velocity of the diffracted waves is 2.7 to 3.0 km/sec, which is slightly higher than in the simulations. This disagreement is not significant because (1) the measurement of the propagation velocity is estimated from a few, closely spaced stations; and (2) the diffracted waves may propagate at an angle with respect to the seismic profile.

Amplification at a Very Steep Ridge

The low amplification at Sourpi lead us to search for another ridge that presents the same advantages as Sourpi, elongated structure of hard rock with hardly any overburden, but one that is much steeper. The purpose was to study whether an extreme topography would produce very high amplifications at the ridge top. In this paragraph, selected results from a such a study will be presented.

Field Work and Data Selection

The ridge, Mont Saint Eynard, is located in the Chartreuse Massif in the French Alps. It is an elongated structure with almost vertical cliffs toward the southeast and a slope of approximately 25° toward the northwest (see Fig. 12). The width of the ridge is 2 to 3 km and its length 7 to 8 km.

Figure 12b shows a simplified geological cross section of the ridge. Upper Jurassic limestone and marl constitute Mt. St. Eynard. The NW slopes of the ridge have hard rock at the surface with a shallow overburden (20 to 40 cm) in a few places. The cliffs toward SE expose over 400 m of homogeneous limestone. Shallow, poorly

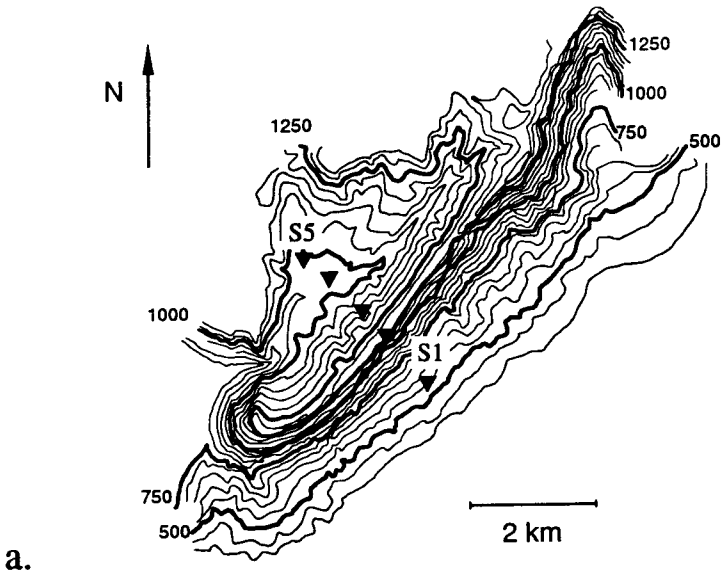

a.

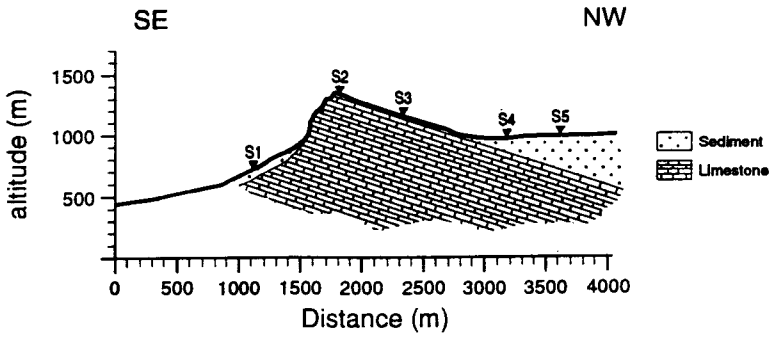

b.

Figure 12. Geometry of Mt. St. Eynard and seismological stations (triangles). (a) Contour map (altitude in meters). (b) Geological cross section and seismic stations.

Table 1
Characteristics of Teleseismic Events. λ—Latitude; ϕ—Longitude; Δ—Epicentral Distance; baz—Backazimuth.

Event (m/d/yr)	λ (°)	ϕ (°)	M_b	Δ (°)	baz (°)
01/23/93	54.509	−161.615	5.7	84.0	352.6
02/02/93	42.212	86.126	5.7	55.8	62.3
02/09/93[a]	−14.438	167.235	4.9	145.5	33.0
02/09/93[b]	45.691	141.929	5.5	81.5	29.4
02/11/93	−20.05	165.39	5.1	149.7	40.5
02/13/93[a]	−14.837	−177.000	5.7	149.6	5.3
02/13/93[b]	51.722	176.467	5.3	83.1	5.8

Table 2
Characteristics of Regional and Local Events. Symbols as in Table 1.

Event (m/d/yr)	λ (°)	ϕ (°)	M_b	Δ (km)	baz (°)
01/27/93	43.445	5.573	—	200	182
02/01/93[a]	44.107	6.967	1.7	160	141
02/01/93[b]	44.626	4.490	1.9	120	233
02/03/93	45.415	5.255	1.4	45	291
02/12/93	44.738	4.557	2.0	110	237

consolidated sediments of unknown thickness are present on both sides of the ridge.

No seismic surveys have been carried out on Mt. St. Eynard and estimates of wave propagation velocities are based on seismic studies of similar limestone in the region. Some of these studies were carried out on fresh, unfractured limestone in quarries. Compressional wave velocities in superficial Upper Jurassic limestone in the area can be high, up to 5.7 km/sec (Thouvenot and Perrier, 1980; Thouvenot and Ménard, 1990). In the case of Mt. St. Eynard, the velocity may be lower as a result of the surface exposure of the rock and the presence of clay in the marls.

During 5 weeks, ground velocity was continuously recorded by five 3D Mark Product L4C seismometers and recorded by REFTEK data logger. The sampling rate was 25 samples per second, the dynamic range 16 bits, and with the internal clock synchronized with GPS. The seismometers were installed along the profile shown in Figure 12a. All the stations were buried to minimize problems with noise due to wind. Two of the stations, S2 and S3, were installed on hard rock sites, S3 on the slope of the mountain and S2 less than 10 m from the edge of the cliff. The three other stations, S1, S4, and S5, were installed on sites with a shallow sedimentary cover.

We used the reports of SISMALP, the regional seismic network in the western Alps, to search for earthquake records in the data. Based on signal to noise ratios, seven teleseismic events (group T) and five local/regional events (group R) were selected for further analysis. The characteristics of these events are shown in Tables 1 and 2. The signal to noise ratios were over 5 between 0.7 and 4 Hz for the records of teleseismic events (typically 10 to 20 between 0.7 and 2.5 Hz and 5 to 10 between 2.5 and 4 Hz) and between 0.7 and 10 Hz for the local/regional events (typically 5 to 6 between 0.7 and 3 Hz, over 10 between 3 and 10 Hz).

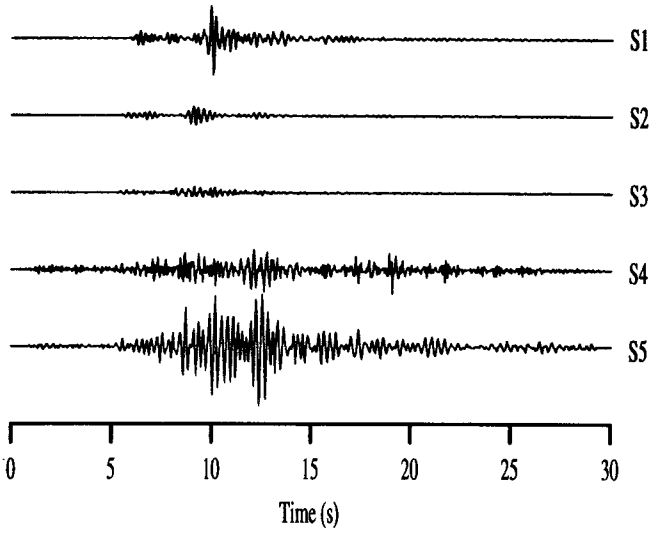

Figure 13. Example of raw data (Z component) from Mt. St. Eynard for a regional event (930203).

Observed Amplifications

An example of raw records of a regional event is shown in Figure 13. It shows that in spite of the steepness of the topography, the amplitude across the array is dominated by effects due to sediments (stations 1, 2, and 5). The amplitudes recorded by stations 1, 2, and 5 were up to an order of magnitude higher than those recorded on hard-rock sites. Effects of the sediments were present down to 1 to 2 Hz, i.e., into the frequency interval where the topographic effects can be expected to be significant.

To study the pure topography-induced effects, stations 2 and 3 were selected for spectral ratio analysis. The most energetic part of the seismic signal was selected by applying a Hanning time window (of length 20 to 40 sec for group T, 20 to 25 sec for group R) to this part of the records. It was not possible to analyze only the first arrival, as the associated time window was too short to get reliable results for sufficiently low frequencies. The spectral amplitude ratio station 3/station 2 was calculated between the spectra smoothed over running windows of 0.2-Hz width. Average spectral ratios and standard deviations of the spectral ratios were calculated for the two groups of events.

Figure 14 shows the average spectral ratios S2/S3 and standard deviations for the seven events of group T and the five events of group R. Only spectral ratios for the vertical and the east–west component were calculated because of a malfunction of the acquisition system at S2 for the north–south component.

For the vertical component (Fig. 14a) of group T, there is a broadband relative amplification between 2 and 4 Hz. The maximum of the average spectral ratio is approximately 2. The east–west component (Fig. 14b) shows relative amplification between 1 and 4 Hz with a maximum of the average spectral ratio of 3.5.

The spectral ratio curves for the vertical component are very similar for events of group T and group R in spite of a larger scatter of individual events in group R (Fig. 14c). There is a larger disagreement between the two groups of events for the east–west component (Fig. 14d), but the general trend of the curves is similar. For the east–west component, the spectral ratios for group R show a larger scatter between individual curves than do those for group T. Furthermore, the average spectral ratio for group R has a distinct peak at 1.5 Hz.

Group R adds information about spectral ratios for frequencies higher than 4 Hz. The spectral ratio for the vertical component is generally lower than one for frequencies over 6 Hz, while the spectral ratio for the east–

west component on average remains at a level not significantly different from one in this frequency interval.

Theoretical Spectral Ratios

In this section, numerical simulations of amplification at Mt. St. Eynard are presented. The method and principle of simulation are the same as those for Sourpi. The model studied corresponds to the cross section of Mt. St. Eynard at the profile through the seismic stations (see Fig. 12b). The wave velocities are 5.2 km/sec for compressional waves and 3 km/sec for shear waves. Spectral ratios were calculated between spectra obtained for locations that correspond to stations S2 and S3. The spectral ratios were calculated after smoothing the two spectra to avoid large peaks due to zero amplitude of the spectrum at S3.

The teleseismic events were located at an epicentral distance between 80° and 150° (see Table 1). The main part of the seismograms consisted of the *P* phase (or the *PKP* phase for distances over 140°) and its coda. The theoretical incidence angle of the *P* waves is between 21° and 27° and the theoretical backazimuths are between 353° and 63°. This corresponds to azimuths between 70° and 140° in the simulations. The simulations of group T, therefore, had incident waves of type *P*, incidence of 25°, and azimuths between 60° and 150° (ϕ = 60°, 90°, 120°, and 150°). The events of group R were located at distances between 40 and 200 km. At these distances, *S*-wave energy dominates the record either in the form of *S* waves or in the form of *Lg* waves that arrive with quite large incidence angles. Backazimuths are very variable: between 140° and 290°. Simulations for group R used incident waves of type *SV*, incidence 45°, and azimuths between 0° and 180° (ϕ = 0°, 30°, 60°, 90°, 120°, 150°, and 180°).

In Figure 14, theoretical spectral ratios from simulations are superposed on the measured spectral ratios. For the vertical component of group T (Fig. 14a), there

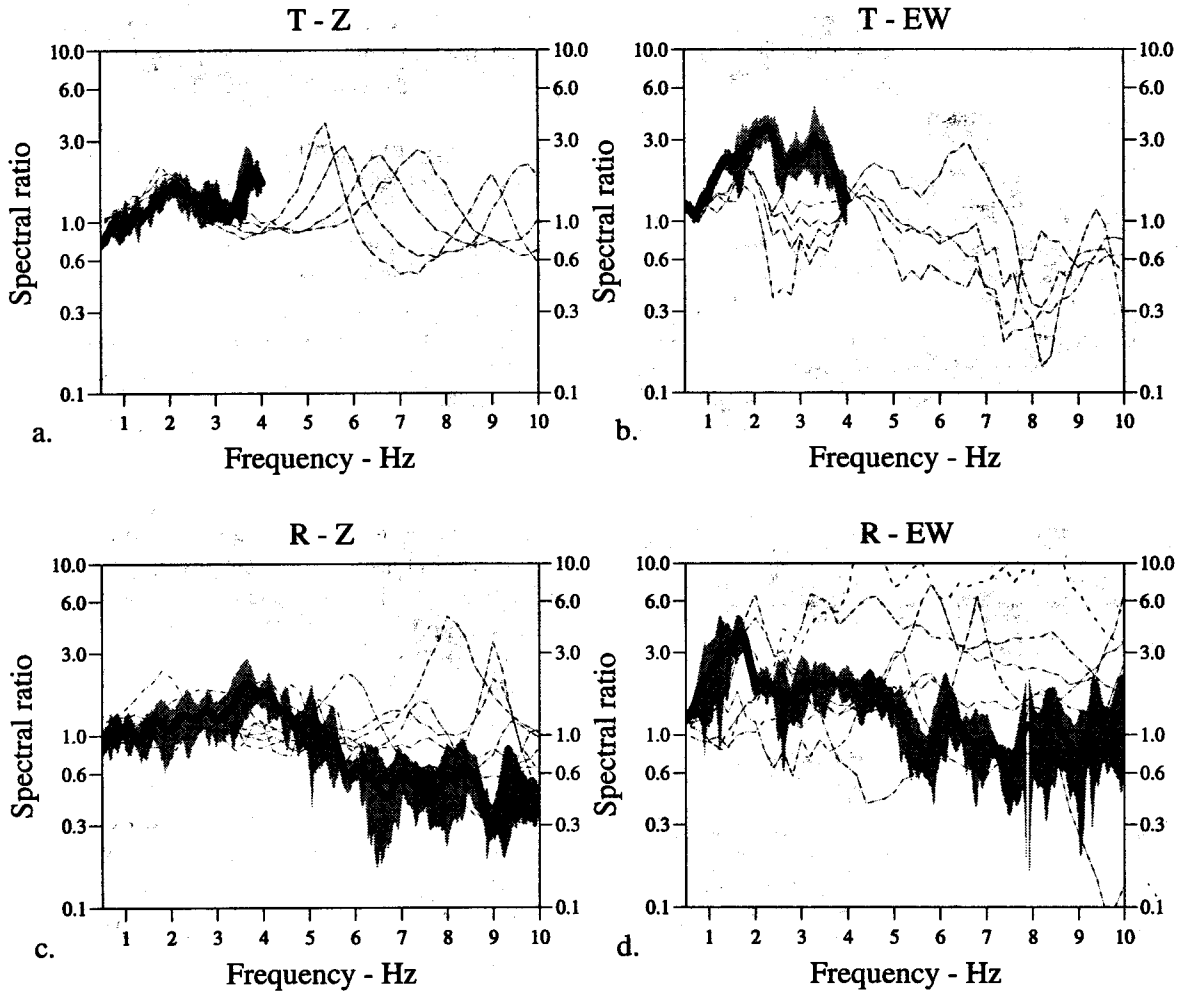

Figure 14. Theoretical spectral ratios S2/S3 (dashed lines), observed spectral ratios S2/S3 (solid lines), and standard deviations of observed spectral ratios (shaded areas). (a) Group T, Z component. (b) Group T, E–W component. (c) Group R, Z component. (d) Group R, E–W component.

is good agreement between theoretical and observed curves even though they differ in details. There is less agreement between the theoretical and the observed spectral ratios for the east–west component (Fig. 14b). This disagreement may be related to the complexity of the incident waves. In fact, the data show as much energy on the horizontal components as on the vertical one, except during the very onset of the *P* (*PKP*) wave, which lasts about 1 sec. Simulations using incident waves that have significant amounts of energy on the horizontal components fit data better for the east–west component. For group R, the simulations show a considerable scatter, but both the general shape of the observed curve and the level of relative amplification are well explained.

Mt. St. Eynard confirms the results from Sourpi: amplification is modest and it is within the range predicted by numerical simulations.

Conclusions

The major conclusion of this study is that in simple cases such as Sourpi and Mt. St. Eynard, there is indeed agreement between observations and numerical simulations concerning the level of amplification due to the topography. The spectral ratio top/base was on average smaller than three at Sourpi (four at Mt. St. Eynard for top/flank) on all components, but peaks of spectral ratios can be present as a result of deamplification at the reference station. The numerical simulations show that absolute amplification takes place at different places for different frequencies, and that in particular an amplification is possible at or close to the top of the ridge. This amplification is generally modest but it can have peak values up to two (compared to the amplitude in the absence of the topography) for certain frequencies.

The agreement between numerical results and observations was further confirmed in the time domain for the Sourpi data, where observed amplifications correspond well to those obtained by numerical simulations, and where data confirmed the theoretical prediction of diffracted waves that propagate from the top toward the base of the ridge.

Our results show that the major problem in data analysis is the lack of a reference station, as site effects due to a topography extend much farther in space than the topography itself. In particular, deamplifications at the reference station can be interpreted as amplifications elsewhere. Another difficulty in the interpretation and theoretical modeling of data is the lack of knowledge on the polarization and nature of the incident waves. The complexity of the incident wave field may explain why the measured spectral ratios presented in this article seem to be unaffected by earthquake locations even though theoretical spectral ratios are significantly affected by the azimuth, incidence, and type of the incoming waves.

Acknowledgments

Special thanks are given to everybody who took part in the field work, in particular D. Legrand, A. Herrero, V. Lignier, P. Verdier, and A. Deschamps. We thank François Glangeaud for his valuable help in the wave separation analysis. SISMALP was of great help by providing us with SISMALP trigger times and epicenter locations. We benefited from logistical support by K. Makropoulos and P. Hatzidimitriou. The work was partially supported by the European Community with Research Grant Number B/EPOCH-913006 and Contract Number EPOCH-CT910043, and by the Délégation au Risques Majeurs of the French Ministry of Environment by Contract Number 91269. Numerical simulations were carried out at the Centre de Calcul Intensif of Observatoire de Grenoble.

References

Anooshehpoor, A. and J. N. Brune (1989). Foam rubber modeling of topographic and dam interaction effects at Pacoima Dam, *Bull. Seism. Soc. Am.* **79**, 1347–1360.

Bard, P.-Y. (1982). Diffracted waves and displacement field over two-dimensional elevated topographies, *Geophys. J. R. Astr. Soc.* **71**, 731–760.

Bard, P.-Y. and B. E. Tucker (1985). Underground and ridge site effects: a comparison of observation and theory, *Bull. Seism. Soc. Am.* **75**, 905–922.

Boore, D. M. (1973). The effect of simple topography on seismic waves: implications for the accelerations recorded at Pacoima Dam, San Fernando Valley, California, *Bull. Seism. Soc. Am.* **63**, 1603–1609.

Bouchon, M. (1973). Effect of topography on surface motion, *Bull. Seism. Soc. Am.* **63**, 615–632.

Bouchon, M. (1985). A simple, complete numerical solution to the problem of diffraction of SH waves by an irregular surface, *J. Acoust. Soc. Am.* **77**, 1–5.

Campillo, M., P.-Y. Bard, F. Nicollin, and F. Sánchez-Sesma (1988). The Mexico earthquake of September 19, 1985—the incident wavefield in Mexico City during the Great Michoacán earthquake and its interaction with the deep basin, *Earthquake Spectra*, **4**, 591–608.

Çelebi, M. (1987). Topographical and geological amplifications determined from strong-motion and aftershock records of the 3 March 1985 Chile earthquake, *Bull. Seism. Soc. Am.* **77**, 1147–1167.

Dainty, A. M. and M. N. Toksöz (1990). Array analysis of seismic scattering, *Bull. Seism. Soc. Am.* **80**, 2242–2260.

Davis, L. L. and L. R. West (1973). Observed effects of topography on ground motion, *Bull. Seism. Soc. Am.* **63**, 283–298.

Freire, S., L. M. Ulrych, and J. Tad (1988). Application of singular value decomposition to vertical seismic profiling, *Geophysics* **53**, 778–785.

Geli, L., P.-Y. Bard, and B. Jullien (1988). The effect of topography on earthquake ground motion: a review and new results, *Bull. Seism. Soc. Am.* **78**, 42–63.

Glangeaud, F. and J. L. Lacoume (1985). Correction of seismic traces by adaptative signal processing, *IASTED Int. Symposium*, Paris, 19–21 June, Proceeding Applied Signal Processing, pp. 263–269.

Glangeaud, F. and D. Latombe (1983). Identification of electromagnetic sources, *Ann. Geophys.* **1–3**, 245–252.

Glangeaud F. and J. L. Mari (1993). Wave separation—part 1, *Revue de l'Institut Francais du Pétrole* **48**, 467–500.

Glangeaud F. and J. L. Mari (1994). *Wave Separation*, Editions Technip, Paris.

Griffiths, D. W. and G. A. Bollinger (1979). The effect of Appalachian mountain topography on seismic waves, *Bull. Seism. Soc. Am.* **69**, 1081–1105.

Kawase, H. (1988). Time-domain response of a semi-circular canyon for incident *SV*, *P*, and Rayleigh waves calculated by the discrete wavenumber boundary element method, *Bull. Seism. Soc. Am.* **79**, 1415–1437.

Kawase, H. and K. Aki (1990). Topography effect at the critical *SV* wave incidence: possible explanation of damage pattern by the Whittier Narrow, California, earthquake of 1 October 1987, *Bull. Seism. Soc. Am.* **80**, 1–22.

Lines, L. R. and S. Treitel (1984). Tutorial: a review of least-squares inversion and its application to geophysical problems, *Geophys. Prospect.* **32**, 159–186.

Luco, J. E., H. L. Wong, and F. C. P. Barros (1990). Three-dimensional response of a cylindrical canyon in a layered half-space, *Int. J. Earthquake Eng. Struct. Dyn.* **19**, 799–817.

Mars, J., F. Glangeaud, F. Lacoume, J. L. Fourmann, and S. Spitz (1987). Separation of seismic waves (expanded abstracts), *57th SEG Meeting*, New Orleans, 11–15 October, 489–492.

Mercier, J. L., E. Carey, H. Philip, and D. Sorel (1976). La néotectonique plioquaternaire de l'arc égéen externe et de la mer Egée et ses relations avec la sismicité, *Bull. Soc. Géol. France* **7**, 355–372.

Mermoz, H. (1976). Imagerie, corrélation et modèles, *Ann. Télécommunications* **31**, 17–36.

Nicollin, F., F. Glangeaud, F. Thouvenot, and M. Lambert (1988). The spectral matrix method applied to explosion seismology data: examples from the Western Alps, *European Geophys. Soc. Meeting*, Bologna, 25–28 March.

Pedersen, H., F. Sánchez-Sesma, and M. Campillo (1994). Three-dimensional scattering by two-dimensional topographies, *Bull. Seism. Soc. Am.* **84**, 1169–1183.

Rogers, A. M., L. J. Katz, and T. J. Bennett (1974). Topographic effects on ground motion for incident *P* waves: a model study, *Bull. Seism. Soc. Am.* **64**, 437–456.

Sánchez-Sesma, F. J., M. A. Bravo, and I. Herrera (1985). Surface motion of topographical irregularities for incident P, SV, and Rayleigh waves, *Bull. Seism. Soc. Am.* **75**, 263–269.

Sánchez-Sesma, F. J. and M. Campillo (1991). Diffraction of *P*, *SV* and Rayleigh waves by topographical features: a boundary integral formulation, *Bull. Seism. Soc. Am.* **81**, 2234–2253.

Sánchez-Sesma, F. J. and M. Campillo (1993). Topographic effects for incident P, SV and Rayleigh waves, *Tectonophysics* **218**, 113–125.

Sánchez-Sesma, F. J. (1983). Diffraction of elastic waves by three-dimensional surface irregularities, *Bull. Seism. Soc. Am.* **73**, 1621–1636.

Sánchez-Sesma, F. J., I. Herrera, and J. Avilés (1982). A boundary method for elastic wave diffraction: application to scattering of *SH* waves by surface irregularities, *Bull. Seism. Soc. Am.* **72**, 473–490.

Thouvenot, F. and G. Ménard (1990). Allochthony of the Chartreuse subalpine massif: explosion-seismology constraints, *J. Struct. Geol.* **12**, 113–121.

Thouvenot, F. and G. Perrier (1980). Seismic evidence of a crustal overthrust in the Western Alps, *Pure Appl. Geophys.* **119**, 163–184.

Trifunac, M. D. and D. E. Hudson (1971). Analysis of the Pacoima Dam accelerogram—San Fernando, California, earthquake of 1971, *Bull. Seism. Soc. Am.* **61**, 1393–1141.

Umeda, Y., A. Kuroiso, K. Ito, and I. Muramatu (1987). High accelerations produced by the Western Nagano Prefecture, Japan, earthquake of 1984, *Tectonophysics* **141**, 335–343.

Wong, H. L. (1982). Effect of surface topography on the diffraction of *P*, *SV*, and Rayleigh waves, *Bull. Seism. Soc. Am.* **72**, 1167–1183.

Wong, H. L. and P. C. Jennings (1975). Effects of canyon topography on strong ground motion, *Bull. Seism. Soc. Am.* **65**, 1239–1257.

Laboratoire de Géophysique Interne et Tectonophysique
Université Joseph Fourier
38041 Grenoble Cedex, France
(H.P., B.L.B., D.H., M.C., P.Y.B.)

Laboratoire Central des Ponts-et-Chaussées
75732 Paris Cedex, France
(P.Y.B.)

Institut Universitaire de France
(M.C.)

Manuscript received 28 March 1994.